J. Fluid Mech. (2011), *vol.* 671, *pp.* 466–490. © Cambridge University Press 2011
doi:10.1017/S0022112010005835

Cellular flow in a small blood vessel

JONATHAN B. FREUND[1]† AND M. M. ORESCANIN[2]

[1]Departments of Mechanical Science and Engineering and Aerospace Engineering, University of Illinois at Urbana-Champaign, Urbana, IL 61801, USA

[2]Department of Mechanical Science and Engineering, University of Illinois at Urbana-Champaign, Urbana, IL 61801, USA

(Received 7 July 2010; revised 24 September 2010; accepted 6 November 2010; first published online 18 February 2011)

In the smallest capillaries, or in tubes with diameter $D \lesssim 8$ μm, flowing red blood cells are well known to organize into single-file trains, with each cell deformed into an approximately static bullet-like shape. Detailed high-fidelity simulations are used to investigate flow in a model blood vessel with diameter slightly larger than this: $D = 11.3$ μm. In this case, the cells deviate from this single-file arrangement, deforming continuously and significantly. At the higher shear rates simulated (mean velocity divided by diameter $U/D \gtrsim 50\,\mathrm{s}^{-1}$), the effective tube viscosity is shear-rate insensitive with $\mu_{eff}/\mu_{plasma} = 1.21$. This matches well with the value $\mu_{eff}/\mu_{plasma} = 1.19$ predicted for the same 30 % cell volume fraction by an established empirical fit of high-shear-rate *in vitro* experimental data. At lower shear rates, the effective viscosity increases, reaching $\mu_{eff}/\mu_{plasma} \approx 1.65$ at the lowest shear rate simulated ($U/D \approx 3.7\,\mathrm{s}^{-1}$). Because of the continuous deformations, the cell-interior viscosity is potentially important for vessels of this size. However, most results for simulations with cell interior viscosity five times that of the plasma ($\lambda = 5$), which is thought to be close to physiological conditions, closely match results for cases with $\lambda = 1$. The cell-free layer that forms along the vessel walls thickens from 0.3 μm for $U/D = 3.7\,\mathrm{s}^{-1}$ up to 1.2 μm for $U/D \gtrsim 100\,\mathrm{s}^{-1}$, in reasonable agreement with reported experimental results. The thickness of this cell-free layer is the key factor governing the overall flow resistance, and this in turn is shown to follow a trend expected for lubrication lift forces for shear rates between $U/D \approx 8\,\mathrm{s}^{-1}$ and $U/D \approx 100\,\mathrm{s}^{-1}$. Only in this same range are the cells near the vessel wall on average inclined relative to the wall, as might be expected for a lubrication mechanism. Metrics are developed to quantify the kinematics of this dense cellular flow in terms of the well-known tank-treading and tumbling behaviours often observed for isolated cells in shear flows. One notable effect of $\lambda = 5$ versus $\lambda = 1$ is that it suppresses treading rotation rates by a factor of about 2. The treading rate is found to scale with the velocity difference across the cell-rich core and is thus significantly slower than the overall shear rate in the flow, which is presumably why the flow is otherwise insensitive to λ. The cells in all cases also have a similarly slow mean tumbling motion, which is insensitive to cell-interior viscosity and decreases monotonically with increasing U/D.

Key words: blood flow, capsule/cell dynamics, particle/fluid flows

† Email address for correspondence: jbfreund@illinois.edu

https://doi.org/10.1017/S0022112010005835 Published online by Cambridge University Press

1. Introduction

In vessels with diameters smaller than around $D = 8\,\mu$m, blood cells are observed to flow down the centre of vessels and advect with little or no change to their apparent axisymmetric bullet-like shape (Skalak & Branemark 1969; Pries & Secomb 2003). In cases there appears to be a mild asymmetry, but an axisymmetric model seems well justified and has been used in both theoretical studies (Secomb 1987) and simulations (Pozrikidis 2005). The steadiness of the cell shape and its position at the centre of the vessel leads to the red cells acting as solid plug-like bodies with layers of Newtonian-fluid plasma between them and the vessel walls. The formation of relatively thick cell-free layers, relative to the vessel diameter, explains the minimum in effective viscosity observed for $D \approx 7\,\mu$m (Pries, Neuhaus & Gaehtgens 1992).

For larger diameter vessels, the cells no longer form single-file trains (Gaehtgens, Duhrssen & Albrecht 1980; Pries & Secomb 2003). Instead, they appear to deform continuously into complex and varied shapes as they interact and move relative to each other. There are still layers of nearly pure plasma along the vessel walls (Alonso *et al.* 1995; Soutani *et al.* 1995; Kim *et al.* 2007), which are consistent with low near-wall viscosity measurements (Long 2004), but the overall dynamics are complex. There is no uniformity of shape or orientation of the cells and detailed experimental diagnostics are challenging at these small scales in blood. Our study is focused on flow at the onset of this apparently more random behaviour. We simulate vessels with $D = 11.3\,\mu$m, which corresponds to the diameter of the vessel being twice that of a sphere with the same volume as a red cell. This D is also just above both the approximately $8\,\mu$m disk diameter of a resting red cell and the diameter for which the effective viscosity is expected to be minimized (Pries *et al.* 1992). The cell motions are expected to significantly deviate from the orderly, single-file behaviour seen in smaller vessels, but since the vessel diameter is only just larger than the cells, the cellular makeup of the fluid is still expected to be a key factor affecting the flow dynamics.

We only consider red cells. In whole blood, they are about 1000 times more prevalent than white cells, and therefore are expected to play a dominant role in blood mechanics, though the somewhat larger size and greater stiffness of white cells might indeed make them dynamically significant in the smallest vessels despite their relatively low concentration (Kamm 2002). There are also platelets in blood, but they are only about $3\,\mu$m in their longest dimension and are outnumbered by red cells by a factor of around 15. They are not therefore expected to be dynamically significant for the flows we study here.

Red cells are relatively simple from a mechanical perspective. Their interior is a haemoglobin-rich solution with no cell nucleus or other organelles, all of which are ejected from the cell early in its formation (Alberts *et al.* 2008). Following Pozrikidis (2003), we model the cell interior as a Newtonian fluid. A precise value for the interior viscosity is unknown, but measurements suggest a value that is only around five times higher than that of the plasma (Dintenfass 1968). The importance of the interior viscosity is unclear. Certainly, it is not expected to be a significant factor in vessels small enough that the cells flow nearly statically in single file, since in this limit there is little or no interior relative motion. However, it will be potentially more important for the larger vessel we simulate. We consider both $\lambda = \mu_{interior}/\mu_{plasma} = 1$ and $\lambda = 5$, the second of which is expected to be the more physiologically realistic and has been used previously (e.g. Pozrikidis 2005).

A red-cell membrane is a nearly constant area because of its high elastic resistance to dilatation (Hochmuth & Waugh 1987), but it is otherwise flexible, with small

https://doi.org/10.1017/S0022112010005835 Published online by Cambridge University Press

enough resistance to shear (Hochmuth & Waugh 1987) and bending (Evans 1983) to deform substantially in blood flow at physiological conditions. At the lowest flow rates we simulate, the cells approximately retain their resting bi-concave shapes, whereas at the highest shear rates, corresponding to the upper range of what is expected physiologically, the cells are highly distorted. The lipids making up the cell membranes are sufficiently mobile to flow as a fluid within the membrane, but the overall viscosity of this membrane is high (Evans & Hochmuth 1976), and it is not clear if its fluid character is important for the overall flow dynamics in small vessels. Membrane viscosity is expected to affect cell relaxation times, as discussed by Pozrikidis (2005), but we neglect it here and still see good agreement with experimental measurements of blood flow in small tubes.

The intriguing rheological characteristics of blood flow in small vessels, which stem from its cellular character, have been widely documented. The Fåhræus–Lindqvist effect (Fåhræus & Lindqvist 1931) is the decrease in effective viscosity with decreasing diameter of the blood vessel. Below $D \approx 7\,\mu\text{m}$, the effective viscosity appears to increase rapidly as the cells must deform more and more significantly to flow through the vessel, even in single file. The related Fåhræus effect refers to a decrease in haematocrit with decreasing vessel diameter (Pries *et al.* 1994; Sharan & Popel 2001). This is also due to the increasing relative thickness of a near-wall plasma-rich layer in smaller diameter vessels. With our simulation model, we examine the effect of cell-interior viscosity and the overall flow rate on the cell-free layer.

Experiments show that in tubes with diameters between about $D = 20\,\mu\text{m}$ and $100\,\mu\text{m}$, the effective viscosity is relatively insensitive to shear rate for mean velocities U such that $U/D > 50\,\text{s}^{-1}$ (Reinke, Johnson & Gaehtgens 1986; Alonso *et al.* 1995). Effective viscosity can increase significantly with decreasing shear rate when red cells aggregate (Reinke, Gaehtgens & Johnson 1987; Alonso *et al.* 1995), which they do more easily at lower shear rates. Suppressing aggregation by altering the suspending fluid can indeed suppress the shear-rate dependence of effective viscosity at lower shear rates (Reinke *et al.* 1987). At low shear rates in capillaries or capillary-scale tubes, the flexibility of the red cells is expected to become relatively more important. It is, for example, essential for describing the single-file flow in the narrowest capillaries (Secomb 1987). Bulk viscometric measurements show that low-shear-rate viscosities match viscosities for hardened red cells, presumably because at low enough shear rates the red cells do not deform significantly and thus behave as rigid bodies (Chien *et al.* 1967). We neglect aggregation and study these factors directly, which are expected to be particularly important in the narrowest vessels. Our simulations are designed to examine the full range of relevant shear rates, from low shears with near-rigid-body behaviour of the cells to the large deformations at the highest physiological shear rates.

Theoretical models suggest that there should be a shear dependence of the effective viscosity in the smallest vessels, especially when cells must deform to even flow through the vessels. The more the cells deform, and thereby increase the thickness of the low-resistance plasma layers along the vessel walls, the more the overall resistance decreases (Secomb 1987, 2003). Our $D = 11.3\,\mu\text{m}$ vessels are harder to model at the outset in this fashion because the packing and deformations of the cells are more challenging to anticipate or describe based upon the limited available experimental observations. This size of vessel in general has been challenging to study experimentally.

The widely observed presence of the near-wall cell-free region (Reinke *et al.* 1987; Alonso *et al.* 1995; Sharan & Popel 2001; Freund 2007; Doddi & Bagchi 2008,

https://doi.org/10.1017/S0022112010005835 Published online by Cambridge University Press

2009; Gidaspow & Huang 2009) has inspired theoretical models for larger vessels as well. In these, fluids with different properties are assumed to represent the cell-rich and cell-depleted regions (Nair, Hellums & Olson 1989; Cokelet & Goldsmith 1991; Sharan & Popel 2001). Generally, these models assume an already separated flow caused by red-cell aggregation (Cokelet & Goldsmith 1991). The plasma viscosity is used for the cell-depleted layer, though a higher viscosity has also been used to model an anticipated increased resistance caused by the expected non-uniform diameter of the cell-rich region (Sharan & Popel 2001). Gupta, Nigam & Jaffrin (1982) include an intermediate layer between the vessel centre and the cell-free layer in which the viscosity increases linearly with distance from the wall. However, it is unclear what fidelity a continuum model could have for vessels such as we study with diameter so similar to the cell size. In summarizing such flow models, Sharan & Popel (2001) point out that both the single-file limit ($D \lesssim 8\,\mu\text{m}$) and flows with $D \gtrsim 20\,\mu\text{m}$ seem to be reasonably well understood, but not the range in between. We study $D = 11.3\,\mu\text{m}$ as a representative of this range. We shall see that even without aggregation a clear cell-free layer forms along the vessel walls and that it is indeed responsible for the apparent low viscosity of the overall flow. The core flow is so compacted by hydrodynamic factors that it ends up with an effective local viscosity many times that expected for blood at the nominal haematocrit of the vessel.

It is unclear what factors determine the thickness of the cell-free layer. Cell aggregation in the core, often induced through the addition of compounds that promote it, clearly enhances cell-free layer thickness (Cokelet & Goldsmith 1991; Kim *et al.* 2009), but shear-induced migration (Phillips *et al.* 1992) and lubrication-like lift forces (Freund 2007) have also been proposed. It is accepted that an increase in the width of the cell-depleted layer results in a decrease in the effective viscosity of blood flow in vessels with $D = 10$ to $40\,\mu\text{m}$ in diameter. However, several studies, including both experimental (Kim *et al.* 2007) and numerical (Freund 2007) efforts, suggest that aggregation is not necessary for the formation of the cell-depleted layer and that inward flow-induced displacement is sufficient. For flow with suppressed cell–cell aggregation, the cell-depleted layer is reported to decrease in width with increasing discharge haematocrit (Sharan & Popel 2001; Kim *et al.* 2007), with decreasing shear rate (Kim *et al.* 2007, 2009) and with decreasing diameter (Sharan & Popel 2001; Kim *et al.* 2007). Cell–cell attraction is not included in our simulation model, yet we observe realistic cell-free layers and examine the hydrodynamics of their formation.

Our numerical microvessel model is introduced in § 2, which includes its detailed physical configuration, a summary of the numerical methods used, and the simulation procedures followed. Sections 3–6 present basic quantitative results, including measures of cell deformations, cell orientations, cell distributions and the net effective tube viscosity. Comparisons with available experimental data are shown to be excellent. Section 7 analyses the cell-free layer from the perspective of lubrication lift forces. The widely discussed tank-treading and tumbling kinematic descriptions of isolated red cells are developed into quantitative metrics applicable to our dense cellular flow and evaluated in § 8. Conclusions are summarized in § 9.

2. Microvessel model

2.1. *Simulation configuration*

The simulation configuration is shown in figure 1. A streamwise periodic round model microvessel of diameter $D = 11.3\,\mu\text{m}$ and length $L = 37.6\,\mu\text{m}$ contains 12 red cells,

https://doi.org/10.1017/S0022112010005835 Published online by Cambridge University Press

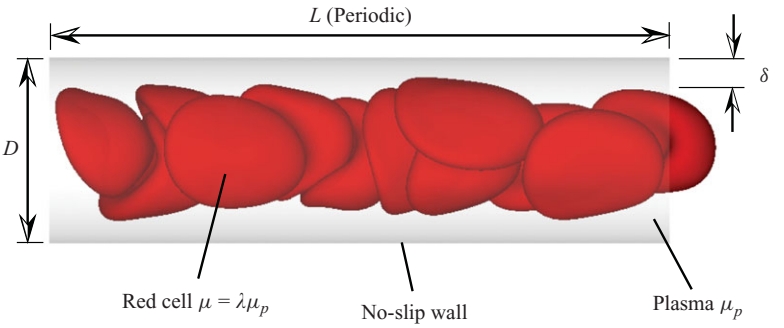


FIGURE 1. (Colour online) Model vessel schematic.

which gives a mean haematocrit of $H_c = 0.30$. A no-slip, no-penetration condition $\boldsymbol{u} = 0$ is enforced on the vessel wall.

The red cells are modelled as neo-Hookean elastic cell membranes, though generalized to have independent shear, dilatation and bending moduli. Full details of our formulation are provided elsewhere (Zhao *et al.* 2010) and follow directly from the red-cell model of Pozrikidis (2005). After Pozrikidis (2005), we take the shear modulus to be $E_s = 4.2 \times 10^{-6}\ \mathrm{N\,m^{-1}}$ and bending modulus to be $E_b = 1.8 \times 10^{-19}\ \mathrm{N\,m}$, both of which are based upon reported measurements. This is a relatively simple model of red-cell mechanics; more detailed measurements (Li *et al.* 2005) have motivated more intricate constitutive models (Dao, Li & Suresh 2006). The near-incompressibility of the cell membranes is enforced with a large dilatational elastic modulus: $E_d = 67.7 \times 10^{-6}\ \mathrm{N\,m^{-1}}$. Even in the most distorting cases we consider, mean surface area variations are less than 6 %. The purely elastic model we employ has been shown to reproduce quantitatively the effective viscosity of dense blood flow in round tubes (Freund & Zhao 2010; Zhao *et al.* 2010).

Blood plasma is accepted to be Newtonian (Whitmore 1968). As discussed in § 1, we compare results for cells with interior viscosity that matches the plasma viscosity ($\lambda = 1$) with results for cells with interior viscosity that is five times greater than the plasma viscosity ($\lambda = 5$).

Because all the fluids are taken to be incompressible, there should be no change in cell volume. Of course, numerical errors can lead to violations of this, and such errors can accumulate in time during a long simulation and lead to significant changes in cell volume. Previously, we have shown that our basic scheme nearly preserves cell volume, even through complex distortions, and that our additional correction keeps volume variations below 0.01 % (Zhao *et al.* 2010).

We consider mean velocities that range from about 40 to $5700\,\mu\mathrm{m\,s^{-1}}$, as seen in table 1. These correspond to pseudo-shear rates of $U/D = 3.7$ to $510\,\mathrm{s^{-1}}$. This range was selected because of its physiological relevance in narrow ($\leqslant 100\,\mu\mathrm{m}$) vessels and because of the change in the rheological behaviour that is expected over this range. Because there are finite changes in the effective viscosity between the $\lambda = 1$ and 5 cases, the pseudo-shear rates do not match exactly. However, they are nearly the same, as can be seen in the table, making it convenient to use the common nominal values listed when discussing results.

The initial condition was configured with red cells of a standard bi-concave shape (Pozrikidis 2003) randomly offset from a regular single-file array. The perturbations

https://doi.org/10.1017/S0022112010005835 Published online by Cambridge University Press

$\mu_{interior}/\mu_{plasma}$	U (μm s^{-1})	U/D (s^{-1})	U/D nominal (s^{-1})	Resolution N
$\lambda=1$	41.5	3.67	3.7	16
	85.5	7.58	7.6	16
	174.6	15.45	15	16
	353.1	31.25	31	16
	713.3	63.13	63	16
	1431	126.6	127	16
	2867	253.7	254	16
	5753	509.2	510	32
$\lambda=5$	41.4	3.66	3.7	16
	85.4	7.76	7.6	16
	173.5	15.35	15	16
	352.3	31.18	31	16
	713.0	63.10	63	16
	1431	126.6	127	16
	2864	253.5	254	24
	5705	504.9	510	32

TABLE 1. Cases simulated.

grew quickly in time, and all simulations are confirmed to be statistically stationary, as discussed in § 2.3.

2.2. *Numerical algorithm*

The Reynolds numbers of flow in the microcirculation are well less than unity, which justifies neglect of the inertia terms in the flow equations. The flow can thus be solved with boundary-integral methods (Pozrikidis 1992), which are implemented using a particle-mesh-Ewald algorithm (Essemann *et al.* 1995) as generalized for Stokes flow by Saintillan, Darve & Shaqfeh (2005). This algorithm is based upon fast Fourier transforms for accurately evaluating long-range hydrodynamic interactions, so the number of operations scales as $O(M \log M)$, with M being the number of surface collocation points on the cells. Alternative approaches for computing long-range interactions within the boundary-integral formulation can yield $O(M)$ overall scaling (e.g. Hernández-Ortiz, de Pablo & Graham 2007), though it is unclear that this nominally better scaling would be advantageous for systems of the size in this study.

Reduced hydrodynamic models (Noguchi & Gompper 2005; Dupin *et al.* 2007; McWhirter, Noguchi & Gompper 2009; Fedosov, Caswell & Karniadakis 2010*a*), where mesosopic particle-collision models are employed, provide opportunities to significantly reduce computational expense on a per-cell basis. Being constructed from a thermal-particle perspective, they also can naturally include thermal fluctuations. Such formulations are also compatible with coarse-grained descriptions of the membrane mechanics (Fedosov, Caswell & Karniadakis 2010*b*). This approach has been used successfully to study the phenomena of red cells and red-cell-like elastic capsules in extensive parametric studies and for relatively large systems (Dupin *et al.* 2007; McWhirter *et al.* 2009; Fedosov *et al.* 2010*a*). However, the inherent modelling approximations of this approach fundamentally diminish fidelity for solving the hydrodynamics. For example, the narrow regions between closely packed cells will not be solved accurately unless they are sufficiently resolved. Similarly, the deformations of cells can be extensive, and sufficient resolution is also required to resolve the relatively sharp features that can form on the membrane. Whether or not these are

https://doi.org/10.1017/S0022112010005835 Published online by Cambridge University Press

important in any particular application is difficult to anticipate. Here we choose a relatively costly high-fidelity approach to resolve both the membrane mechanics and the hydrodynamics. The full details of our formulation along with extensive verification and validation simulations are reported elsewhere (Freund & Zhao 2010; Zhao *et al.* 2010).

The cell shapes are represented by spherical harmonic expansions of the form

$$\boldsymbol{x}(\theta,\phi)=\sum_{n=0}^{N-1}\sum_{m=0}^{n}\bar{P}_n^m(\sin\theta)(\boldsymbol{a}_{nm}\cos m\phi+\boldsymbol{b}_{nm}\sin m\phi), \tag{2.1}$$

where $\boldsymbol{x}$ are points on the membranes in three dimensions, $\bar{P}_n^m$ are the normalized associated Legendre polynomials, and $\boldsymbol{a}$ and $\boldsymbol{b}$ are the corresponding coefficients of the harmonic expansion. This expansion provides uniform resolution over the unit sphere on which the basis functions are defined, as discussed in full for this application elsewhere (Zhao *et al.* 2010). No attempt was made to adapt the mapping to improve resolution of sharp features; the spherical harmonic spectra discussed in § 3 suggest that the deformations are indeed well resolved. The surface forces acting on the fluid due to stresses in the deformed cell membranes are evaluated analytically from this truncated expansion at collocation points on the membrane. Higher shear rates lead to larger cell deformations, which require more terms in this expansion to accurately represent. The resolution used in each case, quantified by N in (2.1), is listed in table 1.

A key advantage of our spherical harmonic discretization, in addition to its spectral resolution properties, is that it facilitates approximate de-aliasing (Canuto *et al.* 1987) of the nonlinear operations needed to calculate the membrane traction. This avoids the spurious buildup of short-wavelength deformations on the cell membranes without degradation of the resolved components of their shape, as must occur to some degree if any explicit or implicit numerical dissipation or filtering is used to stabilize the method. This is also discussed in full elsewhere (Freund 2007; Freund & Zhao 2010; Zhao *et al.* 2010). Numerical tests have shown that with our de-aliasing procedure, the resolution can be set as needed for accuracy goals without regard for stability and that the resolved spectrum is a good model for the modes represented when compared with significantly more resolved computations.

At the haematocrits of interest the cells come into close contact. A key advantage of a boundary-integral formulation is that it can facilitate accurate solution when only thin layers of plasma separate the cells. We do this by switching to a nearly singular formulation of the integrands when surface points on cells are in near proximity (Zhao *et al.* 2010). Though lubrication mechanisms preclude contact in finite time for finite forces, the finite accuracy of the discretization will still, after long times, permit cells to intersect. These rare occurrences are avoided by imposing a constraint on the cell separation: they are artificially separated if they approach closer than 56 nm. This separation distance is only 1 % of the diameter of a sphere matching the volume of the cells. For flow conditions similar to those studied here, pressure drop in a round tube was shown previously to be independent of this model parameter (Zhao *et al.* 2010). This 56 nm constraint is close to the scale at which molecular interactions are expected to become significant. For example, fibrinogen is a 45 nm long (Bachmann *et al.* 1973) molecule present in blood plasma that is known to affect the aggregation properties of red cells (Marton *et al.* 2001) and thereby haemorheology (Chien *et al.* 1967). Thus, it is not clear that such a non-intersection constraint is any less realistic for non-aggregating blood cells than a more precise accounting of the lubrication layers would be.

https://doi.org/10.1017/S0022112010005835 Published online by Cambridge University Press

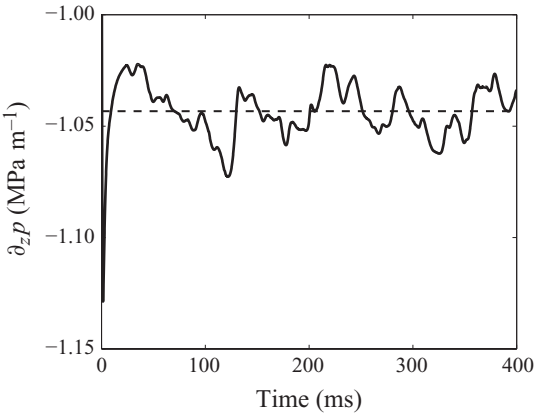


FIGURE 2. Example pressure gradient history for $U/D = 254\,\mathrm{s}^{-1}$, $\lambda = 1$. The straight dashed line represents the selected average pressure gradient.

The vessel walls are discretized with 25 704 triangular surface mesh elements, on which the surface force required to maintain the no-slip condition is computed using second-order accurate linear elements built upon seven-point Gauss quadratures (Pozrikidis 1992). The full details of this are also discussed elsewhere (Zhao *et al.* 2010).

2.3. *Statistical convergence*

Simulations were run until the mean streamwise pressure gradient was independent of the sample size. Trial starting points for establishing this statistical independence were determined by inspecting pressure gradient histories, such as that shown in figure 2. In this case, $t = 100$ ms was assumed to be the end of the initial transient. Over this period, a typical cell traversed around 100 tube diameters or 30 periodic lengths of the tube. This case is shown because it was initiated with a regular array of red cells, perturbed randomly off the centreline of the tube. All other cases were initialized by restarting simulations with the desired flow rates and interior viscosities from realizations of cases with similar properties that had already been deemed to be statistically stationary. This was done to reduce the initial transients they experienced.

3. Cell deformation

Examples of the red-cell shapes and orientations for different cases are shown in figure 3. It is clear that at the lower shear rates the cells are only slightly deformed, remaining close to their well-known bi-concave resting shape. At higher shear rates, they become elongated in the streamwise direction and develop sharper features, thus precipitating the need for higher resolution in these cases. Spectra of the deformation,

$$E_n = \sum_{m=0}^{n} (|\boldsymbol{a}_{nm}|^2 + |\boldsymbol{b}_{nm}|^2), \tag{3.1}$$

show this quantitatively in figure 4(*a*). We see that for the lowest flow rates, the n-odd components are close to those for the symmetric equilibrium resting shape, though deformation is increased somewhat at larger n and there is now small but finite deformation in n-even modes due to small asymmetries cause by the flow. The plot of individual spectral components versus U/D in figure 4(*b*) shows that deformation

https://doi.org/10.1017/S0022112010005835 Published online by Cambridge University Press

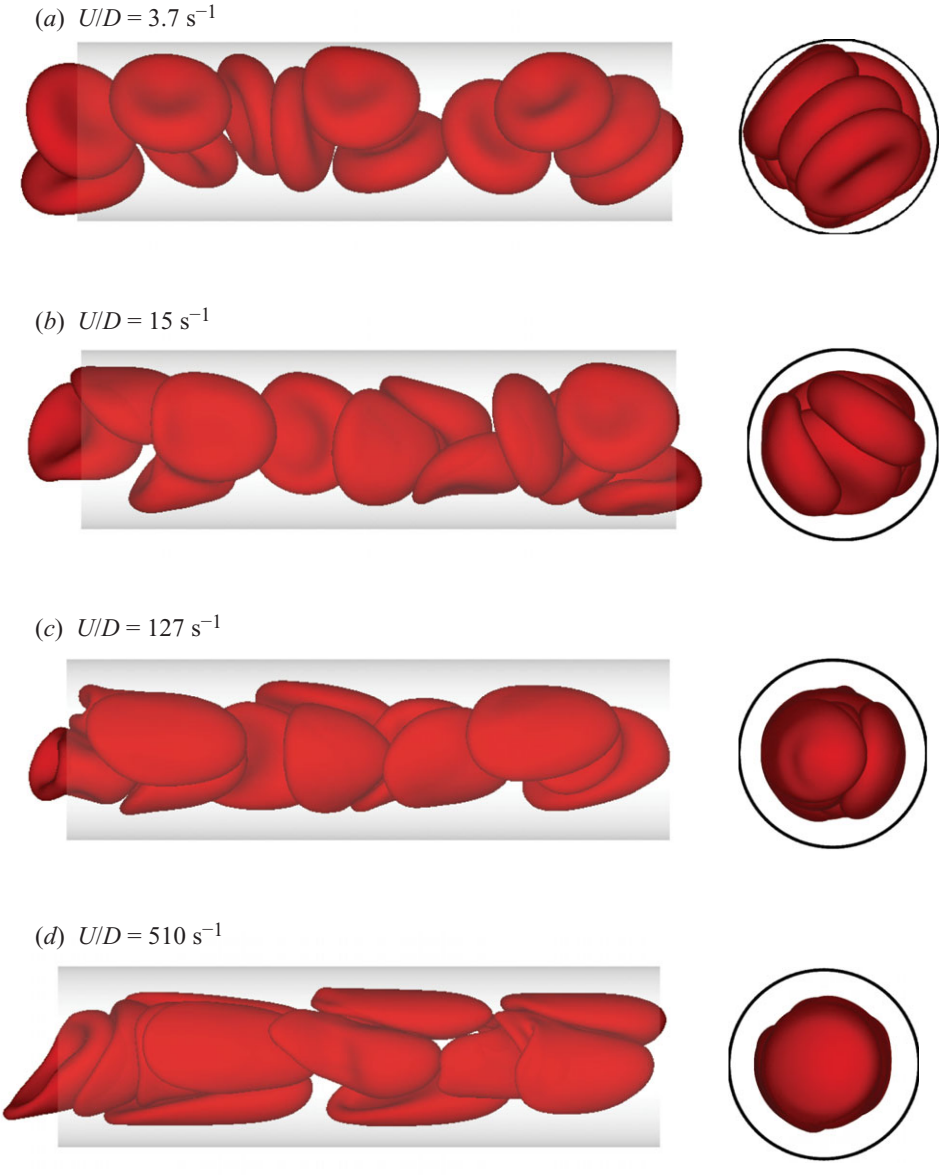


FIGURE 3. (Colour online) Visualizations of example cases as labelled for $\lambda = 5$. Flow is from left to right or towards the viewer.

at these higher mode numbers increases in approximately direct proportion to the pseudo-shear rate. We also see that the deformation is nearly identical for $\lambda = 1$ and 5, though at lower shear rates there is marginally more deformation for the $\lambda = 1$ cases.

It is also clear from the visualizations in figure 3 that at higher shear rates the cells become stretched and oriented in the streamwise direction, whereas at lower shear rates they appear more randomly oriented. This is quantified in figure 5(a–d), which shows the distribution of α, which measures the angle between the radial coordinate

https://doi.org/10.1017/S0022112010005835 Published online by Cambridge University Press

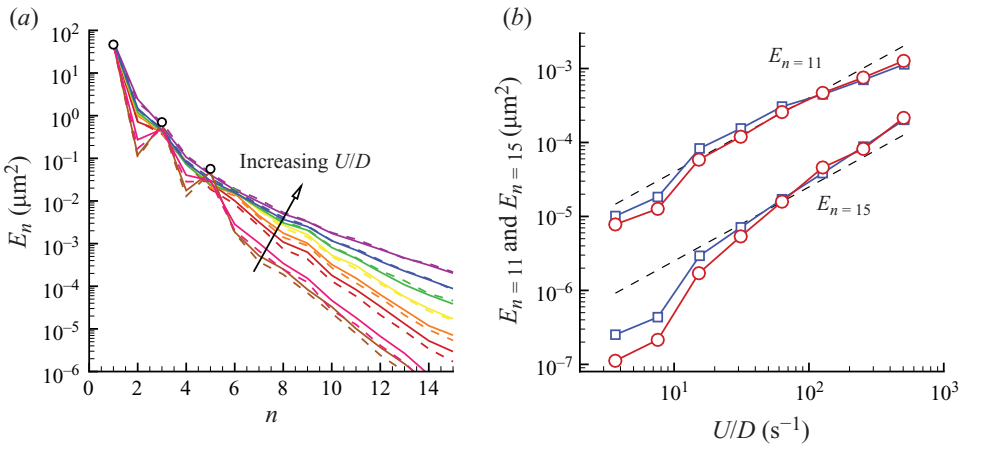


FIGURE 4. (Colour online) (*a*) Time-averaged cell deformation spectra (3.1) for all the cases in table 1: ——— , $\lambda = 1$; – – – –, $\lambda = 5$. For reference, circles show the spectrum of the red-cell equilibrium shape. Only three circle points are seen because the symmetry of this resting configuration causes the n-even points to be zero and because its smoothness leads to $E_n < 10^{-6}$ μm^2 for $n > 5$. (*b*) $E_{n=11}$ and $E_{n=15}$ for all the cases: □, $\lambda = 1$; ○, $\lambda = 5$.

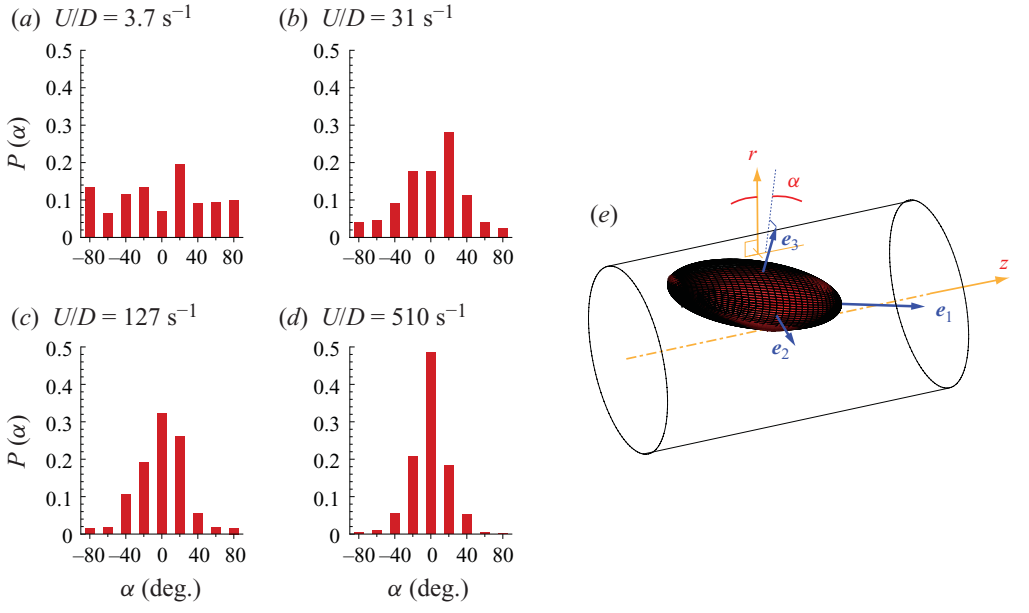


FIGURE 5. (Colour online) (*a–d*) Probability distribution of downstream cell tilt angle for α defined as shown in (*e*) for a typical cell. Cases with $\lambda = 5$ are shown for U/D as labelled.

r extending from the tube axis of symmetry and the projection onto the r–z plane of the eigenvector of

$$M_{ij} = \frac{1}{A}\int_A x_i' x_j' \, \mathrm{d}S(\boldsymbol{x}) \tag{3.2}$$

corresponding to its smallest eigenvalue. In (3.2), A is the surface area of a cell and $\boldsymbol{x}'$ are membrane surface positions relative to the cell centroid. These principal coordinate directions $\boldsymbol{e}_{1,2,3}$, the ellipsoid constructed based on the eigensystem of M_{ij},

https://doi.org/10.1017/S0022112010005835 Published online by Cambridge University Press

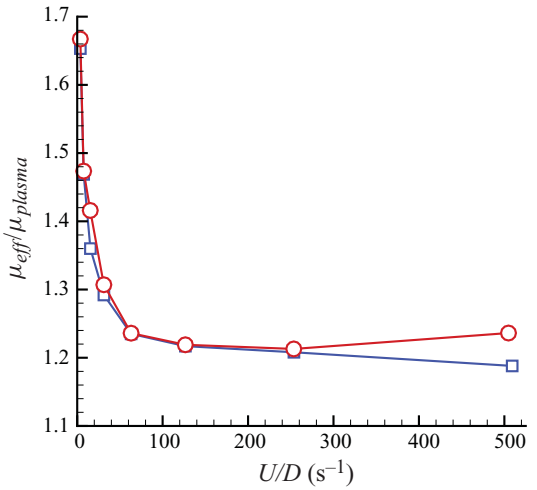


FIGURE 6. (Colour online) Effective relative viscosity for all cases: □, $\lambda = 1$; ○, $\lambda = 5$.

and α are shown for a typical cell in figure 5(*e*). The minor axis of the ellipsoid, labelled $\boldsymbol{e}_3$ in the figure, is selected for measuring this angle since $\boldsymbol{e}_1$ and $\boldsymbol{e}_2$ become ambiguous for slow flow due to the cell symmetry in the effectively rigid-cell limit.

4. Effective viscosity

The net resistance of blood flow in vessels is often quantified by its apparent Poiseuille-flow Newtonian viscosity μ_{eff}, measured relative to the viscosity of the suspending fluid μ_{plasma}. This is easily determined via the Poiseuille law, the mean pressure drop as presented in § 2.3, and the mean flow rate in the tube, as discussed in detail by Zhao *et al.* (2010). It is plotted for all the cases in figure 6. Despite the factor-of-five increase in cell-interior viscosity, the $\lambda = 5$ cases show nearly the same shear-rate dependence as the $\lambda = 1$ cases. For both, μ_{eff}/μ_{plasma} decreases rapidly with increasing U/D at small shear rates and becomes shear-rate insensitive for $U/D \gtrsim 100\,\mathrm{s}^{-1}$, approaching $\mu_{eff}/\mu_{plasma} = 1.21$, which closely matches the value $\mu_{eff}/\mu_{plasma} = 1.19$ predicted by the empirical fit developed by Pries *et al.* (1992) using a database of 163 measurements from 18 high-shear-rate experimental studies. These experimental data were selected such that $U/D > 50\,\mathrm{s}^{-1}$ and a majority of the cases had $U/D < 500\,\mathrm{s}^{-1}$. The biggest difference between the $\lambda = 1$ and $\lambda = 5$ cases is at the highest shear rate $U/D = 509\,\mathrm{s}^{-1}$, with the $\lambda = 5$ case increasing to $\mu_{eff}/\mu_{plasma} = 1.23$ and the $\lambda = 1$ case continuing an apparently slow decrease to $\mu_{eff}/\mu_{plasma} = 1.19$, but even here the difference is clearly small. It does not seem possible to assess agreement with experiment more precisely since the experimental data generally vary by $\pm 10\,\%$ around the empirical fits (Pries *et al.* 1992).

The shear-rate dependence of the effective viscosity for flow in tubes and vessels with diameters between $D = 8$ and $20\,\mu\mathrm{m}$ is not extensively documented. In larger tubes ($\gtrsim 20\,\mu\mathrm{m}$) and in absence of significant aggregation, there appears to be little or no shear-rate sensitivity for pseudo-shear rates above $1\ \mathrm{s}^{-1}$ (Reinke *et al.* 1986, 1987; Alonso *et al.* 1995). However, for $D = 11.3\,\mu\mathrm{m}$ we see a marked increase in μ_{eff}/μ_{plasma} with decreasing U/D for $U/D \lesssim 100\,\mathrm{s}^{-1}$. This increase is more similar to that observed in vessels with $D < 8\,\mu\mathrm{m}$, as summarized by Secomb (1987). The

https://doi.org/10.1017/S0022112010005835 Published online by Cambridge University Press

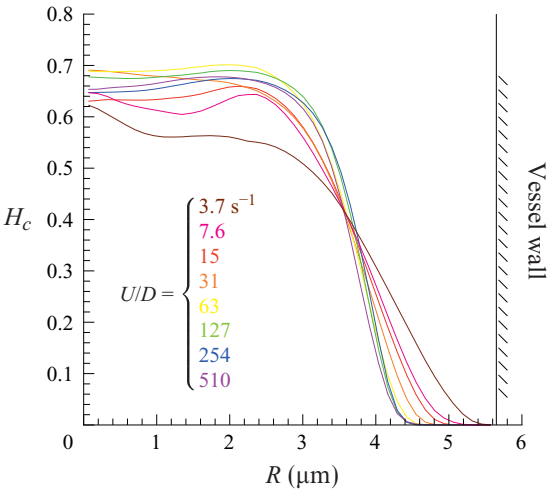


FIGURE 7. (Colour online) Radial haematocrit profiles for all the $\lambda = 1$ cases.

resistance measured in these smallest vessels increases by a factor of about four as U/D decreases from around 200 s^{-1} down to around 2 s^{-1}, which is thought to result from reduced deformations of the cells in this limit. Here, we see a behaviour that is intermediate between that reported for $D \gtrsim 20\,\mu$m vessels and $D \lesssim 8\,\mu$m vessels: an increase by a factor of about 1.4 as U/D decreases from 100 s^{-1} down to 4 s^{-1}.

5. Local haematocrit

The dynamics of blood flow in small tubes is closely tied to the distribution of the cells, which we quantify with the local haematocrit profile in the vessel:

$$H_c(r) = \frac{1}{2\pi LT} \int_0^T \int_0^L \int_0^{2\pi} \rho(r, \theta, z, t)\, \mathrm{d}\theta\, \mathrm{d}z\, \mathrm{d}t, \tag{5.1}$$

where $\rho = 1$ inside cells and $\rho = 0$ in the plasma, and T is the time over which the flow is deemed to be statistically stationary, as discussed in § 2.3. The radius r, angle θ and streamwise coordinate z make up a cylindrical coordinate system centred on the vessel axis of symmetry (see figure 5*e*). Haematocrit profiles are shown in figure 7. All show a distinct drop in red-cell concentration towards the vessel walls corresponding to the well-documented near-wall cell-free layer, which is also clear in the visualizations of figure 3.

We define the thickness δ of the cell-free layer as shown in figure 1 such that $H_c(D/2 - \delta) = 0.01$. All of the following trends are insensitive to this choice of threshold. For low shear rates, we see in figure 8 that δ increases with increasing U/D, but becomes approximately constant for $U/D \gtrsim 100\,\mathrm{s}^{-1}$. This is similar to many studies that show δ increasing with U/D for non-aggregating cells (Reinke *et al.* 1987; Yamaguchi, Yamakawa & Niimi 1992; Alonso *et al.* 1995; Kim *et al.* 2009). We compare with an empirical fit of measured cell-free-layer thickness versus diameter for vessel diameters ranging from $D = 10$ to $40\,\mu$m (Kim *et al.* 2007). This fit gives $\delta = 0.98\,\mu$m for $D = 11.3\,\mu$m, which is reasonably close to our value of $\delta = 1.2\,\mu$m, though their conditions only approximately match ours. The systemic haematocrit for the data fitted by Kim *et al.* (2007) was 0.42, which suggests that the local haematocrit

https://doi.org/10.1017/S0022112010005835 Published online by Cambridge University Press

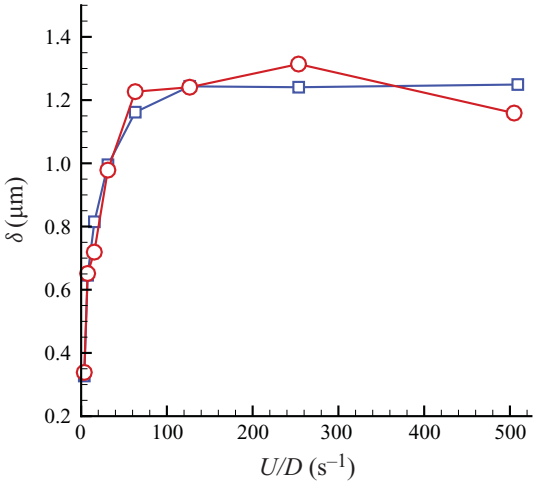


FIGURE 8. (Colour online) Cell-free layer thickness defined by $H_c(D/2-\delta)=0.01$: □, $\lambda=1$; ○, $\lambda=5$.

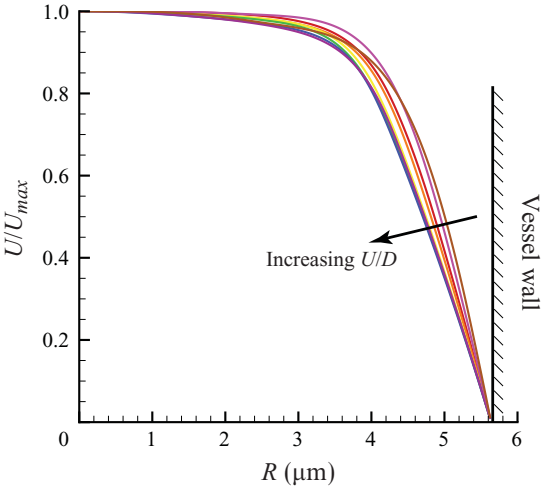


FIGURE 9. (Colour online) Velocity profiles for the $\lambda=5$ cases.

at the point of measurement might have been higher than the mean $H_c=0.30$ in the present study. This discrepancy would be expected to decrease δ. Soutani *et al.* (1995) similarly measured a cell-free layer thickness of about 1 μm (on average) for D around 10 μm for $H_c=0.30$ blood in saline. Evaluating the empirical fit of their considerably scattered data for $D=11.3\,\mu\text{m}$ yields $\delta=0.89\pm0.4\,\mu\text{m}$. Our high-shear-rate value $\delta=1.2\,\mu\text{m}$ is also in this range.

6. Velocity

The velocity profiles for all the $\lambda=5$ cases are plotted in figure 9. The profiles become more blunted with decreasing U/D, with the only exception to this being the slowest flowing $U/D=3.7\,\text{s}^{-1}$ case, which seems to have its own distinct character. Here the cells are in effect nearly rigid, barely deformed by the flow (figure 3), and the

https://doi.org/10.1017/S0022112010005835 Published online by Cambridge University Press

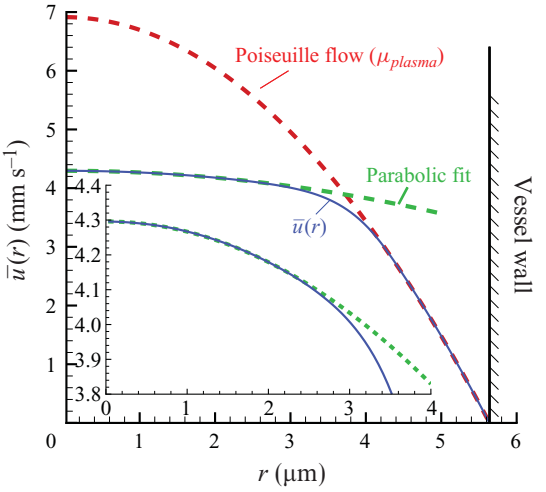


FIGURE 10. (Colour online) Velocity profile for the $U/D = 254\,\mathrm{s}^{-1}$, $\lambda = 1$ case. The inset shows the same data with a vertical scale that emphasizes the limited range of inner parabolic fit.

velocity profile appears to become more rounded as the cell-free layer thickness drops to near zero (figure 8). On the basis of visualized cell motion in a 12 μm diameter tube, Gaehtgens *et al.* (1980) anticipated blunted velocity profiles.

Figure 10 shows an example of how close to the wall the velocity profile matches the parabola that would be predicted for Poiseuille flow of a fluid with the plasma viscosity. However, towards the centre of the vessel, profiles flatten substantially. Parabolas can be fitted to this flattened region as shown, but the fits are poor except perhaps for the higher flow rate cases, such as shown in figure 10. No effective Newtonian viscosities could be deduced using a consistent procedure for all cases, and a Newtonian viscosity is not even expected in the core region. Nevertheless, all measures suggest that core viscosities are at least a factor of 10 higher than the plasma viscosity, meaning that the interior flow might be modelled as rigid relative to the plasma layer for some applications.

7. Lubrication lift forces and the cell-free layer

The effective viscosity becomes constant at higher shear rates owing to the insensitivity of the cell-free layer thickness to shear rate in this limit. Thus, understanding the mechanisms of overall flow resistance is tantamount to understanding what factors lead to the thickness of the near-wall cell-free layer. In the visualizations of figure 3, we see that in addition to becoming streamwise oriented at larger U/D, the cells at the edge of the cell-free layer also become significantly flattened. The relative thinness of this layer and the relative flatness of the cells suggest that the lubrication limit of the flow equations might provide a reasonable model for the hydrodynamic forces that thicken this layer. For such a lubrication mechanism, the wall-normal lifting pressure should follow the well-known scaling of Reynolds (1886),

$$\mathscr{P}_{lub} \propto \frac{U}{\delta^2}, \tag{7.1}$$

which for constant δ at fixed flow conditions should be balanced by a wall-directed force generated somehow in the cell-rich core. A lubrication mechanism would also

https://doi.org/10.1017/S0022112010005835 Published online by Cambridge University Press

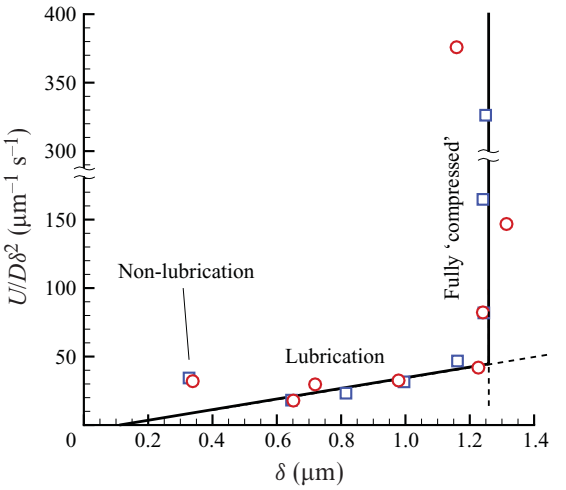


FIGURE 11. (Colour online) Lubrication scaling of the cell-free layer thickness: □, $\lambda = 1$; ○, $\lambda = 5$. The straight solid lines indicate the expected behaviour in the limits as labelled.

require a streamwise asymmetry in the near-wall cell orientation: on average they would need to be inclined in the streamwise direction. The visualizations of figure 3 also suggest such an orientation, especially for the middle range of the U/D cases shown (figure 3*b*, *c*).

In two dimensions, the thickness of the cell-free layer, at least for the thin layers simulated, was seen to approximately follow a lubrication scaling: $\delta \propto \sqrt{U}$ (Freund 2007). This would be consistent with an approximately constant expansive force due to cellular interactions in the cell-rich core. Messlinger *et al.* (2009) recently showed a similar force–elevation dependence near a wall for two-dimensional fluid-filled elastic capsules. In the present case, a greater range of velocities are studied and the change in the cell-free layer thickness is a more significant fraction of the vessel diameter. We thus expect the expansion force to be a function of $\mathscr{P}_{exp}(\delta)$ as the cells there are compacted and interact more strongly. For sufficiently small changes in δ, this should be approximately linear relative to some fixed reference value $\mathscr{P}(\delta_o) = \mathscr{P}_o$: $\mathscr{P}_{exp} = \mathscr{P}_o + K\delta$, where $K = \partial_\delta \mathscr{P}(\delta_o)$. However, we can also anticipate that this linear model must fail as the core becomes increasingly resistant to confinement as the cells become more closely packed or interact more strongly.

To assess this, we assume that at the edge of the cell-free layer, lubrication lift forces (7.1) exactly balance a spring-like resistance to confinement. The expansion pressure $\mathscr{P}_{exp}$ is thus in balance with the lubrication lift: $\mathscr{P}_{exp} = \mathscr{P}_{lub}$. For a linear-spring-like resistance of the cell-rich core to compression, we expect $\mathscr{P}_o + K\delta = C\delta$, where C is the constant of proportionality in (7.1). We also expect that $\mathscr{P}_{exp}$ should rise significantly for δ larger than some critical compression or for flow faster than some critical rate. Both these behaviours are indeed seen in figure 11. For $\delta = 0.6\,\mu$m up to about $1.2\,\mu$m, $U/D\delta^2$ is approximately linearly proportional to δ. Beyond this, there is no further compression. The lowest U/D case does not fit within this picture. In this limit, the cells are in effect nearly rigid and do not flatten towards the walls as would be needed for the lubrication approximation to apply (see figure 3*a*). We expect them to behave almost as rigid particles making up a viscous suspension, for which there is little theoretical guidance.

https://doi.org/10.1017/S0022112010005835 Published online by Cambridge University Press

The abruptness of the transition between the apparent lubrication–linear-spring regime and the full-compression regime is striking, but perhaps not entirely unexpected. The cells are so easily deformed by the flow at the higher speeds simulated that their constant area and constant volume constraints presumably become relatively more important for their dynamic evolution, independent of their shear and bending elasticity. The deformation of the cells continues to increase at the highest U/D shear rates, as seen most clearly in the plots of spectra (figure 4). However, this is most notable at high mode numbers, and given the relative amount of elastic energy associated with such deformations, this elastic energy is relatively small. It is also noteworthy that the packing does not increase to $H_c = 1$, its theoretical maximum, but remains $H_c \lesssim 0.7$ (figure 7). The resistance to packing must therefore be associated with the flow dynamics and motions of the cells in the cell-rich core, not just to elastic packing. This further supports the idea that it is the hydrodynamic interactions of the cells that counter the lubrication factors compressing them. Yet it is unclear if it is an increasing resistance to compression in the core flow itself or a breakdown of the inward lubrication forces due to a change of near-wall cell geometry that leads to this. The near-wall cell geometry is investigated next; the kinematics of cells in the core flow are investigated more fully in the following section.

For lubrication-like factors to contribute to the thickness of the cell-free layer, the cells on average must have a streamwise asymmetry, tilted upward in the direction of the flow. We assess this by computing the average cell inclination angle α, as it is defined in § 3. Small positive α indicates that the ellipsoid fitted to the cell shape forms a thin wedge-shape region between the cell and the vessel wall, resembling a standard slider-bearing configuration. The schematic diagram in figure 5(*e*) shows such an orientation, with the wedge-shaped lubricating fluid layer atop the cell for the orientation shown. The α distributions in figure 5(*a–d*) suggest a slight mean tilt towards positive α for the middle range of the simulated shear rates, but these distributions include all the cells in the vessel. Only the cells near the walls, at the edge of this cell-free layer, are relevant for lubrication lifting. Selecting an objective wall-closeness threshold is challenging because δ changes from case to case and the cells change shape, generally becoming thinner in the wall-normal direction at higher shear rates. We therefore, somewhat arbitrarily, choose the half of the cells whose centroids are closest to the vessel walls and average over these to compute a mean inclination angle $\bar{\alpha}_{1/2}$. The results are plotted for the $\lambda = 5$ case in figure 12. The four cases that fall on the straight line in figure 11 all have relatively large and positive $\bar{\alpha}_{1/2}$, which supports the potential importance of lubrication mechanisms in this regime. The other four cases have relatively small or even negative $\bar{\alpha}_{1/2}$. Switching the averaging criterion changes these results in detail, but not this general conclusion. Negative $\bar{\alpha}_{1/2}$ are unexpected, but not prohibited and might be an artefact of the approximations made. The defined tilt angle is based on a single metric of the complex cell shapes, and thus cannot completely represent lubrication effects for any particular shape. Furthermore, the lubrication theory discussed assumes steady flow, which is only approximately true for the cells, and is even then only an approximate solution of the full governing equations. It is expected to fail as the lubricating layer becomes thicker.

8. Tumbling and tank treading

Tumbling and so-called tank-treading behaviour is widely observed and discussed in regard to dilute suspensions of red cells (Abkarian, Faivre & Viallat 2007; Skotheim

https://doi.org/10.1017/S0022112010005835 Published online by Cambridge University Press

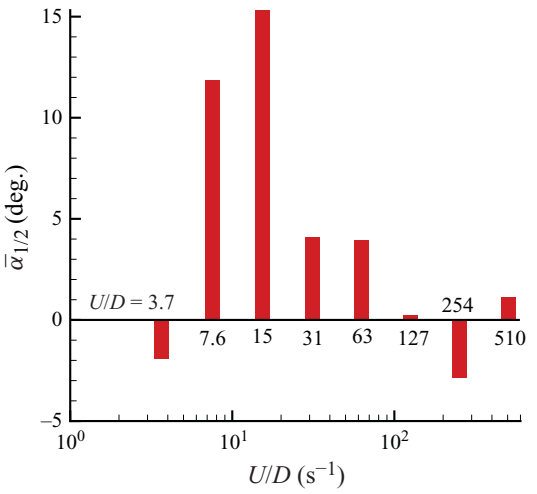


FIGURE 12. (Colour online) The average α for cells close to the vessel wall, defined as in figure 5(*e*), for the $\lambda = 5$ cases.

& Secomb 2007; Sui *et al.* 2008; Doddi & Bagchi 2009). Here we investigate these motions for our confined and realistically dense cellular flow. For what we designate pure tank treading, the cell maintains its shape while material points on its membrane cycle around its surface. Likewise, pure tumbling is a rigid-body-like flipping motion of the cell. These motions are easy to visualize and to discuss qualitatively for isolated cells. To investigate them quantitatively here, we must first define metrics that are applicable in the dense and confined flows we consider.

8.1. *Tumbling and treading metrics*

For cells in isolation, metrics corresponding to tumbling and treading behaviours are easily established. However, the large deformations and complex shapes of the cells flowing under physiological conditions render simple metrics impractical to implement. Further complicating our assessment, we cannot expect cells in a dense flow to ever simply tank-tread or tumble. To be descriptive, however, our metrics should also unambiguously indicate that these limits were the cells in isolation.

To assess the apparent rigid-body-like rotation of a tumbling cell, we define a rigid-body rotation vector $\boldsymbol{\omega}$ based on the ellipsoid constructed from the principal axes $\boldsymbol{e}^{(k)}$ ($k = 1, 2, 3$) of the membrane shape. If a cell maintains its shape but tumbles, this fitted ellipsoid, calculated as discussed in § 3, will tumble with this same $\boldsymbol{\omega}$. Figure 13 shows examples of fitted ellipsoids.

The time rate of change of any vector $\boldsymbol{e}$ fixed to the fitted ellipsoid depends upon $\boldsymbol{\omega}$ as

$$\dot{\boldsymbol{e}} = \boldsymbol{\omega} \times \boldsymbol{e}. \tag{8.1}$$

Taking the cross-product of each side with $\boldsymbol{e}$ and summing the corresponding expressions for the three principal unit vectors $\boldsymbol{e}_i$ yields an invertible 3×3 system to solve for $\boldsymbol{\omega}$:

$$\left[3\boldsymbol{\delta} - \sum_{i=1}^{3} \boldsymbol{e}_i \boldsymbol{e}_i\right] \cdot \boldsymbol{\omega} = \sum_{i=1}^{3} \boldsymbol{e}_i \times \dot{\boldsymbol{e}}_i, \tag{8.2}$$

https://doi.org/10.1017/S0022112010005835 Published online by Cambridge University Press

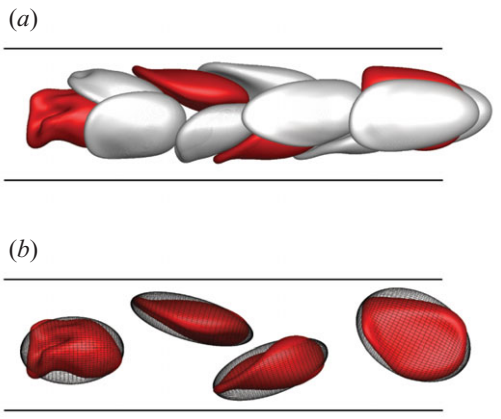


FIGURE 13. (Colour online) Visualization of the $U/D = 254$, $\lambda = 5$ case: (*a*) all the cells and (*b*) selected cells from (*a*) shown with their fitted ellipsoids.

where $\boldsymbol{\delta}$ is the identity tensor. With (8.2), $\boldsymbol{\omega}$ is easily calculated by accurately finite-differencing the time history of the orthonormal $\boldsymbol{e}$ of M_{ij} to compute $\dot{\boldsymbol{e}}$.

Tank treading is a rotation of the membrane without a corresponding rotation of the basic shape of the cell. In this sense, it is a rotation in deviation from the rigid-body-like rotation that defines $\boldsymbol{\omega}$. To quantify this, we employ a definition for membrane angular rotation rate $\boldsymbol{\Omega}$ based upon its instantaneous velocity distribution, and design this rotation rate to match (8.2) for pure tumbling. We thus take $\boldsymbol{\Omega}$ for membrane A to satisfy

$$\boldsymbol{I} \cdot \boldsymbol{\Omega} = \int_A \boldsymbol{v}' \times \boldsymbol{x}' \, \mathrm{d}S(\boldsymbol{x}), \tag{8.3}$$

where $\boldsymbol{v}'$ and $\boldsymbol{x}'$ are velocities and positions relative to those of the cell centroid. Because of its role in dynamics, $\boldsymbol{I}$ is called the inertia tensor and has components

$$I_{ij} = \delta_{ij} \mathrm{tr}(\boldsymbol{A}) - A_{ij}, \tag{8.4}$$

where A_{ij} matches M_{ij} in (3.2) except for the area normalization:

$$A_{ij} = \int_A x_i' x_j' \, \mathrm{d}S(\boldsymbol{x}). \tag{8.5}$$

Here $\boldsymbol{I}$ serves only a kinematic function of recovering rigid-body rotation in that limit. Thus, for pure rigid-body rotation $\boldsymbol{\Omega} = \boldsymbol{\omega}$. For pure tank treading $\boldsymbol{\Omega} \neq 0$, though $\boldsymbol{\omega} = 0$ in this case since the orientation of the cell remains fixed. Faster treading corresponds to larger $|\boldsymbol{\Omega} - \boldsymbol{\omega}|$.

We consider three examples to demonstrate these definitions and confirm our implementation. All are initialized with a red cell near the wall of a diameter $D = 16.9\,\mu\mathrm{m}$ circular tube of streamwise periodic length $L = 22.6\,\mu\mathrm{m}$. The cell's axis of symmetry is parallel to that of the tube and its centroid is positioned at $r = 3.9\,\mu\mathrm{m}$. The flow is in the positive z-direction. The mean velocity in the entire periodic domain is $U = 2.82\,\mathrm{mm\,s^{-1}}$ and the peak velocity on the cells is therefore approximately twice this.

For a tumbling example, we take the viscosity inside the cell to be $\lambda = 10^4$ times that of the suspending plasma, which ensures that the cell will advect with negligible

https://doi.org/10.1017/S0022112010005835 Published online by Cambridge University Press

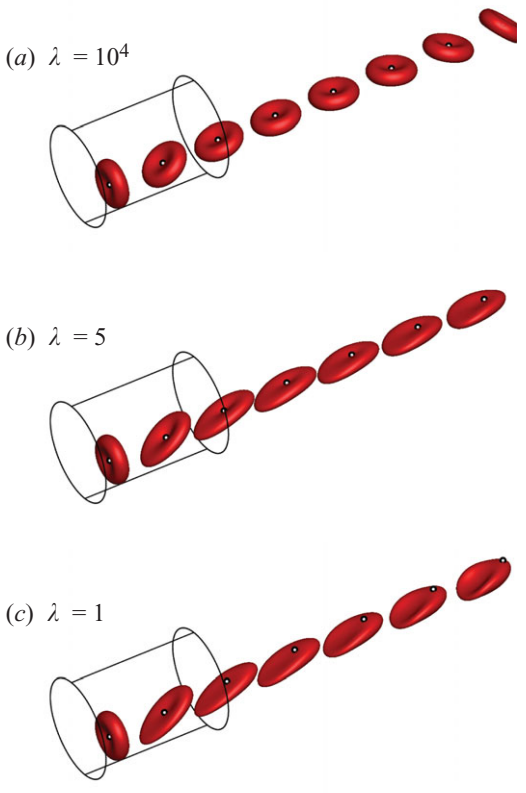


FIGURE 14. (Colour online) The motion of a single cell for the viscosity ratios as labelled. The dot on the cell membrane marks a material point that started on its axis of symmetry. The wire frame shows the periodic length of the tube walls. Consecutive images are spaced in time by $\Delta t = 2$ ms.

distortion over the course of our simulation. For this case, we also stretch the cell by 5 % normal to the vessel wall at its nearest point to remove degeneracy of the eigensystem of $\boldsymbol{A}$ imposed by the perfect symmetry. Figure 14(a) shows the subsequent tumbling of the cell. The corresponding ω_θ and Ω_θ are confirmed to match in figure 15, so the treading metric is indeed zero, $\boldsymbol{\Omega} - \boldsymbol{\omega} = 0$.

Example tank-treading cases are constructed by setting the internal viscosity of the cell to be $\lambda = 5$ and $\lambda = 1$, with greater treading expected for the less viscous $\lambda = 1$ case. Figures 14(b) and 14(c) visualize the subsequent evolution of these model cells. In both cases, after an initial reorientation, the cell shapes become relatively stable though the membrane itself clearly continues to rotate. This treading rotation, as measured by $\Omega_\theta - \omega_\theta$, is plotted in figure 15. The initial tumble is clearly seen in this plot as well as the markedly different behaviour between these nominally tank-treading cells versus the tumbling cell with $\lambda = 10^4$. Treading is suppressed, as expected, for the $\lambda = 5$ cell versus the $\lambda = 1$ cell, being approximately one third of that for the $\lambda = 1$ case.

8.2. *Tumbling and tank-treading results*

Figure 16 shows the treading and tumbling behaviour for all the multi-cell cases simulated, averaged both in time and over all the cells. As the flow rate increases,

https://doi.org/10.1017/S0022112010005835 Published online by Cambridge University Press

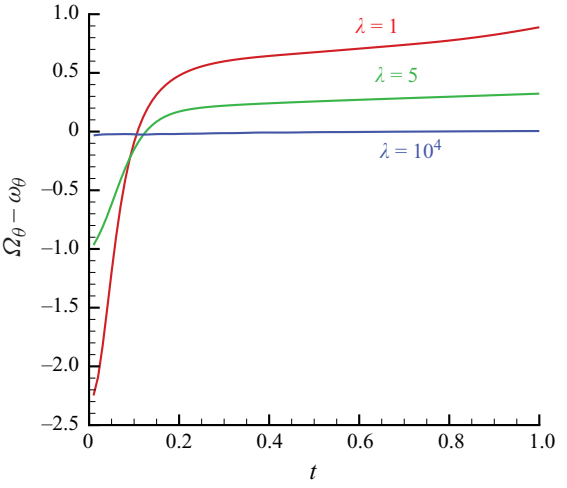


FIGURE 15. (Colour online) The tank-treading metric for cases discussed and visualized in figure 14.

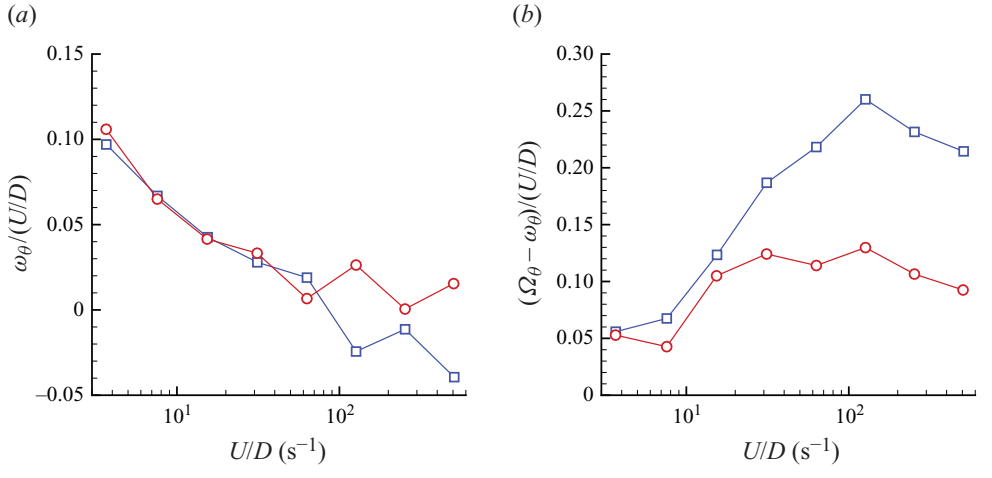


FIGURE 16. (Colour online) Red-cell tumbling and treading metrics: □, $\lambda = 1$; ○, $\lambda = 5$.

we see a similar decrease in tumbling for both interior viscosities (figure 16*a*). This is anticipated based upon the expected decreasing relative role of the membrane elasticity. For smaller U/D, the relatively strong membrane elasticity tends to preserve the cell shape, making it effectively more rigid and therefore more prone to tumbling. Interestingly, the tumbling metric becomes negative for the largest U/D cases with $\lambda = 1$. This is a slow rotation counter to the mean shear of the flow.

Treading generally follows an opposite trend, for the most part increasing with increasing U/D for small U/D (figure 16*b*). This treading metric, however, levels out for $U/D \gtrsim 50$ for the $\lambda = 5$ cases and decreases at the highest shear rates for both $\lambda = 1$ and 5. As expected, there is always less treading for $\lambda = 5$ versus $\lambda = 1$, presumably because of the increased interior viscosity. As the cells become flatter and thinner

https://doi.org/10.1017/S0022112010005835 Published online by Cambridge University Press

at larger U/D, this viscous interior resistance to treading is expected to be further augmented relative to the $\lambda = 1$ case, which is also consistent with the behaviour seen in figure 16(b).

Tumbling that is counter to the mean shear as seen for large U/D in figure 16(a) might be unexpected. However, this simply corresponds to a cell whose leading edge appears to turn towards the centre of the tube, which can occur even though the cell membrane has a net rotation in the opposite direction. It is Ω_θ in (8.3) that can be considered the net rotation rate of the cell membrane, and it is the membrane that satisfies the no-slip condition and is therefore expected to rotate on average with the mean shear in the flow. Comparing the results in figures 16(a) and 16(b) shows that $\Omega_\theta - \omega_\theta$ is indeed always positive and therefore consistent with the cell membrane rotating on average with the mean shear.

While these trends are interesting, and potentially important for some effects, all the treading and tumbling rotation rates are relatively small compared with the overall vessel shear rate. A cell spanning one-half of the vessel, not slipping with the vessel wall, and moving at U in the centre would have an angular rotation rate of $2U/D$, which is approximately 10 times the tumbling and treading rates we see in figure 16. In general, both cell rotation rates better correspond to the velocity difference between the centre of the vessel and the edge of the cell-free layer. We see in the velocity profiles of figures 9 and 10 that less than about 10 % of the drop in velocity between its peak at the vessel centre to the vessel walls occurs in the cell-rich core. Estimates based upon this velocity difference are thus consistent with the rotation rates seen in figure 16. Gaehtgens & Schmid-Schönbein (1982) measured a similarly slow treading rate for the more organized flow of red cells in a 8.5 μm diameter tube. Theoretical studies of still smaller tubes ($D \leqslant 7\,\mu$m) also predict a slow treading rate that does not appear to be an important factor in the overall pressure drop in the tube (Hsu & Secomb 1989). These basic findings thus seem to extend to the present larger tubes, where the cellular disorganization makes simple diagnostics and theoretical analysis more challenging.

It is the tank-treading behaviour of the cells that appears to better correlate with the apparent changes in flow regime identified in the previous section. Tumbling (figure 16a) decreases monotonically and relatively consistently with increasing U/D. Tank-treading behaviour, however, is more complex. In the lubrication regime suggested by figure 11, treading increases for $\lambda = 1$ or remains approximately constant for $\lambda = 5$. However, at large U/D, for which there is no further increase in δ, tank treading becomes suppressed, for both the $\lambda = 1$ and $\lambda = 5$ cases (figure 16). This might be a signature of whatever core-flow hydrodynamic interactions lead to the large U/D behaviour seen in figure 11. In isolation, tank-treading cells tend to become inclined to the vessel wall (figures 14b and 14c), as we see in the near-wall cells in the apparent lubrication regime (figure 12). A reduction in treading is thus also consistent with a failure of lubrication lift at larger U/D.

9. Conclusions

Actual red cells are, of course, expected to be more complex than the Newtonian fluid finite-deformation shell model we employed here. However, our model closely matched measured values of the effective viscosity for flow in small tubes. It also provided reasonable agreement with the limited data reported for the thickness of the cell-free layer and its dependence on flow rate. These results support it being a

https://doi.org/10.1017/S0022112010005835 Published online by Cambridge University Press

reasonably accurate model for the dynamics of dense cellular blood flows in small tubes.

We see that for the smallest shear rates considered ($U/D \lesssim 10\,\mathrm{s}^{-1}$) the cells approximately maintain their characteristic bi-concave equilibrium shape. Spectra show that the energy in the higher spherical harmonics representing the cell increases approximately linearly with increasing shear rate. At high shear rates, the cells flatten substantially and lengthen in the streamwise direction, developing relatively sharp features, especially at their trailing edges. The degree of deformation was insensitive to the factor of five increase in cell interior viscosity.

The computed velocity profiles were seen to be blunt: the near-wall velocity profile matched the parabolic profile expected for Newtonian flow at the plasma viscosity, and the interior profile becomes nearly flat, constituting less than about 10 % of the overall change in velocity across the vessel diameter. It is clear that the effective viscosity of the cell-rich core is many times that of the plasma, and it would probably be reasonably well modelled as rigid in cases. The transition between the cell-free-layer parabola and the nearly uniform flow region is abrupt, extending over only about 1 μm.

For $U/D \lesssim 100\,\mathrm{s}^{-1}$, it was seen that the cell-free layer thickened by a factor of nearly four with increasing shear rate. This occurred in a nearly identical fashion for the $\lambda = 1$ and $\lambda = 5$ cases. The dependence of this thickness upon U/D suggests that in the range $U/D \approx 8\,\mathrm{s}^{-1}$ up to $U/D \approx 100\,\mathrm{s}^{-1}$, the thickness of the cell-free layer was consistent with lubrication effects and a linearly 'compressible' cell-rich core. This view was also consistent with the mean tilt of the cells close to the wall: on average an asymmetric wedge-shaped region forms consistent with expectations for lubrication lift. The cause of the breakdown of this behaviour at larger U/D appears to be hydrodynamic, rather than elastic, in origin since the cells remain far from fully packed at even the highest flow rates. Whether hydrodynamic interactions make the core flow more resistant to compaction or disrupt the cell shapes generating the lubrication lift forces is unclear, but the apparent decrease of tank-treading behaviour is consistent with the latter.

Metrics were designed to quantify cell tumbling and tank treading, but the prominent tumbling and tank treading commonly reported for isolated cells is not seen in this dense and confined flow. With increasing shear rate, tumbling decreases monotonically, which is an expected consequence of the declining relative importance of elasticity and thereby reduced relative cell rigidity. Tank treading increases at small flow rates, especially for cases with matched interior–exterior viscosity ($\lambda = 1$), but falls in both cases at high shear rates, corresponding to the shear rate for which the cell-free layer achieves its maximum thickness. The rates of treading and tumbling were slow relative to the full vessel shear rates; their rate better corresponds to the small velocity drop between the vessel centre and the outer edge of the cell-free layer.

Support from NSF (CBET 09-32607) is gratefully acknowledged.

REFERENCES

Abkarian, M., Faivre, M. & Viallat, A. 2007 Swinging of red blood cells under shear flow. *Phys. Rev. Lett.* **98**, 188302.

Alberts, B., Johnson, A., Lewis, J., Raff, M., Roberts, K. & Walter, P. 2008 *Molecular Biology of the Cell*, 5th edn. Garland Science.

https://doi.org/10.1017/S0022112010005835 Published online by Cambridge University Press

Alonso, C., Pries, A. R., Kiesslich, O., Lerche, D. & Gaehtgens, P. 1995 Transient rheological behavior of blood in low-shear tube flow: velocity profiles and effective viscosity. *Am. J. Physiol. Heart Circ. Physiol.* **268**, H25–H32.

Bachmann, L., Schmitt-Fumain, W. W., Hammel, R. & Lederer, K. 1973 Size and shape of fibrinogen. Part 1. Electron microscopy of the hydrated molecule. *Die Makromol. Chem.* **176** (9), 2603–2618.

Canuto, C., Hussaini, M. Y., Quarteroni, A. & Zang, T. A. 1987 *Spectral Methods in Fluid Dynamics*. Springer.

Chien, S., Usami, S., Dellenback, R. J. & Gregersen, M. I. 1967 Blood viscosity: influence of erythrocyte aggregation. *Science* **157** (3790), 829–831.

Cokelet, G. R. & Goldsmith, H. L. 1991 Decreased hydrodynamic resistance in the two-phase flow of blood through small vertical tubes at low flow rates. *Circ. Res.* **68**, 1–17.

Dao, M., Li, J. & Suresh, S. 2006 Molecularly based analysis of deformation of spectrin network and human erythrocyte. *Mater. Sci. Engng* C **26**, 1232–1244.

Dintenfass, L. 1968 Internal viscosity of the red cell and a blood viscosity equation. *Nature* **219**, 956–958.

Doddi, S. K. & Bagchi, P. 2008 Lateral migration of a capsule in a plane Poiseuille flow in a channel. *Intl J. Multiphase Flow* **34**, 966–986.

Doddi, S. K. & Bagchi, P. 2009 Three-dimensional computational modeling of multiple deformable cells flowing in microvessels. *Phys. Rev.* E **79**, 046318.

Dupin, M. M., Halliday, I., Care, C. M., Alboul, L. & Munn, L. L. 2007 Modeling the flow of dense suspensions of deformable particles in three dimensions. *Phys. Rev.* E **75**, 066707.

Essemann, U., Perera, L., Berkowitz, M. L., Darden, T., Lee, H. & Pedersen, L. G. 1995 A smooth particle mesh Ewald method. *J. Chem. Phys.* **103** (19), 8577–8593.

Evans, E. A. 1983 Bending elastic modulus of red blood cell membrane derived from buckling instability in micropipet aspiration tests. *Biophys. J.* **43**, 27–30.

Evans, E. A. & Hochmuth, R. M. 1976 Membrane viscoelasticity. *Biophys. J.* **16**, 1–11.

Fåhræus, R. & Lindqvist, T. 1931 The viscosity of the blood in narrow capillary tubes. *Am. J. Physiol.* **96**, 562–568.

Fedosov, D. A., Caswell, B. & Karniadakis, G. E. 2010*a* A multiscale red blood cell model with accurate mechanics, rheology, and dynamics. *Biophys. J.* **98**, 2215–2225.

Fedosov, D. A., Caswell, B. & Karniadakis, G. E. 2010*b* Systematic coarse-graining of spectrin-level red blood cell models. *Comput. Meth. Appl. Mech. Engng* **199** (29–32), 1937–1948.

Freund, J. B. 2007 Leukocyte margination in a model microvessel. *Phys. Fluids* **19** (3), 023301.

Freund, J. B. & Zhao, H. 2010 A fast high-resolution boundary integral method for multiple interacting blood cells. In *Computational Hydrodynamics of Capsules and Biological Cells* (ed. C. Pozrikidis), pp. 71–111. Chapman & Hall/CRC.

Gaehtgens, P., Duhrssen, C. & Albrecht, K. H. 1980 Motion, deformation, and interaction of blood cells and plasma during flow through narrow capillary tubes. *Blood Cells* **6**, 799–812.

Gaehtgens, P. & Schmid-Schönbein, H. 1982 Mechanisms of dynamic flow adaptation of mammalian erythrocytes. *Naturwissenschaften* **69**, 294–296.

Gidaspow, D. & Huang, J. 2009 Kinetic theory based model for blood flow and its viscosity. *Ann. Biomed. Engng* **37**, 1534–1545.

Gupta, B. B., Nigam, K. M. & Jaffrin, M. Y. 1982 A three-layer semi-empirical model for flow of blood and other particulate suspensions through narrow tubes. *J. Biomech. Engng* **104**, 129–135.

Hernández-Ortiz, J. P., de Pablo, J. J. & Graham, M. D. 2007 Fast computation of many-particle hydrodynamic and electrostatic interactions in a confined geometry. *Phys. Rev. Lett.* **98**, 140602.

Hochmuth, R. M. & Waugh, R. E. 1987 Erythrocyte membrane elasticity and viscosity. *Annu. Rev. Phys.* **49**, 209–219.

Hsu, R. & Secomb, T. W. 1989 Motion of nonaxisymmetric red blood cells in cylindrical capillaries. *J. Biomech. Engng* **111**, 147–151.

Kamm, R. D. 2002 Cellular fluid mechanics. *Annu. Rev. Fluid Mech.* **34**, 211–32.

Kim, S., Kong, R. L., Popel, A. S., Intaglietta, M. & Johnson, P. C. 2007 Temporal and spatial variations of cell-free layer with arterioles. *Am. J. Physiol. Heart Circ. Physiol.* **293**, H1526–H1535.

https://doi.org/10.1017/S0022112010005835 Published online by Cambridge University Press

Kim, S., Ong, P. K., Yalcin, O., Intaglietta, M. & Johnson, P. C. 2009 The cell-free layer in microvascular blood flow. *Biorheology* **46**, 181–189.

Li, J., Dao, M., Lim, C. T. & Suresh, S. 2005 Spectrin-level modeling of the cytoskeleton and optical tweezers stretching of the erythrocyte. *Biophys. J.* **88**, 3707–3719.

Long, D. S. 2004 Microviscometric analysis of microvascular hemodynamics in vivo. PhD thesis, University of Illinois at Urbana-Champaign, Urbana, Illinois.

Marton, Z., Kesmarky, G., Vekasi, J., Cser, A., Russai, R., Horvath, B. & Toth, K. 2001 Red blood cell aggregation measurements in whole blood and in fibrinogen solutions by different methods. *Clin. Hemorheol. Microcirc.* **24** (2), 75–83.

McWhirter, J. L., Noguchi, H. & Gompper, G. 2009 Flow-induced clustering and alignment of vesicles and red blood cells in microcapillaries. *Proc. Natl Acad. Sci.* **106**, 6039–6043.

Messlinger, S., Schmidt, B., Noguchi, H. & Gompper, G. 2009 Dynamical regimes and hydrodynamic lift of viscous vesicles under shear. *Phys. Rev.* E **80**, 011901.

Nair, P. K., Hellums, J. D. & Olson, J. S. 1989 Prediction of oxygen transport rates in blood flowing in large capillaries. *Microvasc. Res.* **38**, 269–285.

Noguchi, H. & Gompper, G. 2005 Shape transitions of fluid vesicles and red blood cells in capillary flows. *Proc. Natl Acad. Sci.* **102** (40), 14159–14164.

Phillips, R. J., Armstrong, R. C., Brown, R. A., Graham, A. L. & Abbott, J. R. 1992 A constitutive equation for concentrated suspensions that accounts for shear-induced particle migration. *Phys. Fluids* A **4** (1), 30–40.

Pozrikidis, C. 1992 *Boundary Integral and Singularity Methods for Linearized Viscous Flow*. Cambridge University Press.

Pozrikidis, C. 2003 Numerical simulation of the flow-induced deformation of red blood cells. *Ann. Biomed. Engng* **31**, 1194–1205.

Pozrikidis, C. 2005 Axisymmetric motion of a file of red blood cells through capillaries. *Phys. Fluids* **17**, 031503.

Pries, A. R., Neuhaus, D. & Gaehtgens, P. 1992 Blood viscosity in tube flow: dependence on diameter and hematocrit. *Am. J. Physiol. Heart Circ. Physiol.* **263**, H1770–H1778.

Pries, A. R. & Secomb, T. W. 2003 Rheology of the microcirculation. *Clin. Hemorheol. Microcirc.* **29**, 143–148.

Pries, A. R., Secomb, T. W., Gessner, T., Sperandio, M. B., Gross, J. F. & Gaehtgens, P. 1994 Resistance to blood flow in microvessels in vivo. *Circ. Res.* **75**, 904–915.

Reinke, W., Gaehtgens, P. & Johnson, P. C. 1987 Blood viscosity in small tubes: effect of shear rate, aggregation and sedimentation. *Heart Circ. Physiol.* **253**, H540–H547.

Reinke, W., Johnson, P. C. & Gaehtgens, P. 1986 Effect of shear rate variation on apparent viscosity of human blood in tubes of 29 to 94 μm diameter. *Circ. Res.* **59**, 124–132.

Reynolds, O. 1886 On the theory of lubrication and its application to Mr Beauchamp Tower's experiments, including an experimental determination of the viscosity of olive oil. *Proc. R. Soc. Lond.* **177**, 157–234.

Saintillan, D., Darve, E. & Shaqfeh, E. S. G. 2005 A smooth particle-mesh Ewald algorithm for Stokes suspension simulations: the sedimentation of fibers. *Phys. Fluids* **17**, 033301.

Secomb, T. W. 1987 Flow-dependent rheological properties of blood in capillaries. *Microvasc. Res.* **34**, 46–58.

Secomb, T. W. 2003 Mechanics of red blood cells and blood flow in narrow tubes. In *Modeling and Simulation of Capsules and Biological Cells* (ed. C. Pozrikidis), pp. 163–196. Chapman & Hall/CRC.

Sharan, M. & Popel, A. S. 2001 A two-phase model for flow of blood in narrow tubes with increased effective viscosity near the wall. *Biorheology* **38**, 415–428.

Skalak, R. & Branemark, P.-I. 1969 Deformation of red blood cells in capillaries. *Science* **164**, 717–719.

Skotheim, J. M. & Secomb, T. W. 2007 Red blood cells and other nonspherical capsules in shear flow: oscillatory dynamics and tank-treading-to-tumbling transition. *Phys. Rev. Lett.* **98**, 078301.

Soutani, M., Suzuki, Y., Tateishi, N. & Maeda, N. 1995 Quantitative evaluation of flow dynamics of erythrocytes in microvessels: influence of erythrocyte aggregation. *Am. J. Physiol. Heart Circ. Physiol.* **268**, H1959–H1965.

https://doi.org/10.1017/S0022112010005835 Published online by Cambridge University Press

Sui, Y., Chew, Y. T., Roy, P., Cheng, Y. P. & Low, H. T 2008 Dynamic motion of red blood cells in simple shear flow. *Phys. Fluids* **20**, 1–10.

Whitmore, R. L. 1968 *Rheology of the Circulation*. Pergamon.

Yamaguchi, S., Yamakawa, T. & Niimi, H. 1992 Cell-free plasma layer in cerebral microvessels. *Biorheology* **29**, 251–260.

Zhao, H., Isfahani, A. H. G., Olson, L. & Freund, J. B. 2010 A spectral boundary integral method for flowing blood cells. *J. Comput. Phys.* **229** (10), 3726–2744.

https://doi.org/10.1017/S0022112010005835 Published online by Cambridge University Press